Mapping the SO2 Shoreline in Gas Giant Exoplanets

The Astrophysical Journal, 994:184 (11pp), 2025 December 1 https://doi.org/10.3847/1538-4357/ae17cb

Mapping the SO_2 Shoreline in Gas Giant Exoplanets

Ian J. M. Crossfield[1,2], Eva-Maria Ahrer[2], Jonathan Brande[1], Laura Kreidberg[2], Joshua Lothringer[3], Caroline Piaulet-Ghorayeb[4,10], Jesse Polman[5], Luis Welbanks[6], James Kirk[7], Diana Powell[8], and Niloofar Khorshid[9]
[1] Department of Physics and Astronomy, University of Kansas, Lawrence, KS, USA; ianc@ku.edu
[2] Max-Planck-Institut für Astronomie, Königstuhl 17, D-69117 Heidelberg, Germany
[3] Space Telescope Science Institute, Baltimore, MD 21218, USA
[4] Department of Astronomy & Astrophysics, University of Chicago, 5640 South Ellis Avenue, Chicago, IL 60637, USA
[5] Division of Space Research and Planetary Sciences, Physics Institute, University of Bern, Gesellschaftsstrasse 6, 3012 Bern, Switzerland
[6] School of Earth and Space Exploration, Arizona State University, Tempe, AZ, USA
[7] Department of Physics, Imperial College London, Prince Consort Road, London SW7 2AZ, UK
[8] Department of Astronomy & Astrophysics, University of Chicago, Chicago, IL 60637, USA
[9] Department of Space, Earth and Environment, Chalmers University of Technology, Gothenburg, 412 96, Sweden
Received 2025 June 10; revised 2025 September 24; accepted 2025 October 24; published 2025 November 25

Abstract

JWST has revealed sulfur chemistry in giant exoplanet atmospheres, where molecules such as sulfur dioxide (SO_2) trace photochemistry, metallicity, and formation and migration. To ascertain the conditions that determine whether (or how much) SO_2, H_2S, and other sulfur-bearing species are present in exoplanet atmospheres, we present a grid of planetary atmospheres covering metallicities from 0.3 to 1000× solar and temperatures from 250 to 2050 K. These models map out the "SO_2 shoreline," the region of metallicity and irradiation for which SO_2 may be sufficiently abundant to be detectable. SO_2 is a sensitive indicator of metallicity; expected SO_2 abundances also depend strongly on overall temperature and C/O ratio; the SO_2 abundance depends surprisingly weakly on X-ray and ultraviolet irradiation, also weakly on K_{zz} (for $T_{eq} \gtrsim 600$ K), and is essentially independent of internal temperature. Despite its detection in a growing number of giant planets, SO_2 is never the dominant sulfur-bearing molecule: depending on temperature and metallicity, H_2S, S_2, NS, SO, SH, and even S_8 or atomic S are frequently as common (or more so) as SO_2. Nonetheless SO_2 remains the most easily detectable sulfur-bearing species, followed by H_2S, though perhaps SO and SH could be detectable in some gas giants. Aside from a pressing need for additional observational constraints on sulfur, we also identify the need for future work to account for the effects of clouds and hazes, fully self-consistent atmospheric models, 2D and 3D models, a wider range of planetary masses and radii, and studies to measure and refine reaction rates and molecular opacities of sulfur-bearing species.

Unified Astronomy Thesaurus concepts: Astrochemistry (75); Chemical abundances (224); Molecular reactions (2226); Exoplanet atmospheres (487); Exoplanet atmospheric composition (2021); Infrared spectroscopy (2285); Spectroscopy (1558)

1. Introduction

The unexpected presence of sulfur dioxide (SO_2) has been one of the biggest surprises to emerge from JWST's early spectroscopy of gas giants. This molecule burst onto the scene with the Early Release Science transmission spectroscopy of WASP-39b (L. Alderson et al. 2023; Z. Rustamkulov et al. 2023). SO_2 was soon found to result from at least two separate disequilibrium photochemistry pathways at high altitude in hydrogen-rich atmospheres, catalyzed by high-energy ($\lambda < 230$ nm) stellar photons that convert dissociate parent species to ultimately form SO_2 (J. Polman et al. 2023; S.-M. Tsai et al. 2023a; W. de Gruijter et al. 2025; R. Veillet et al. 2025). This exciting new absorber has since been seen in planets with sizes from 0.4 to 1.6 R_J and temperatures from 600 to 1700 K (T. G. Beatty et al. 2024; A. Dyrek et al. 2024). Its triatomic structure makes it a sensitive metallicity tracer, and its photochemical origin means it may also diagnose vertical mixing (e.g., via the eddy diffusion coefficient K_{zz}), internal heat (T_{int}), UV-induced photochemistry, atmospheric dynamics, and planet formation history (S. Constantinou et al. 2023; I. J. M. Crossfield 2023; S.-M. Tsai et al. 2023a; N. Khorshid et al. 2024). However, many mysteries remain.

To date SO_2 has been detected in only four exoplanets. Though first observed at its 4.1 μm ($\nu_1 + \nu_3$) combination band (L. Alderson et al. 2023; Z. Rustamkulov et al. 2023; S.-M. Tsai et al. 2023a), SO_2 and the physical conditions it diagnoses also reveal themselves at the longer-wavelength 7–9 μm ν_1 and ν_3 stretch vibration bands (D. Powell et al. 2024). While SO_2 is seen in hot Jupiters WASP-39b and WASP-107b and in the smaller HAT-P-26b, at both 4.1 and 7–9 μm (L. Alderson et al. 2023; A. Dyrek et al. 2024; D. Powell et al. 2024; D. K. Sing et al. 2024; L. Welbanks et al. 2024; J. Valenti et al. 2025, L. Alderson et al. 2025, in preparation, A. Gressier et al. 2025), the only other planet with detected SO_2, warm Neptune GJ 3470b, exhibits it in the weaker 4.1 μm band but lacks longer-wavelength data (T. G. Beatty et al. 2024).

Beyond SO_2, H_2S (with no associated SO_2) has been seen in the canonical hot Jupiter HD 189733b (G. Fu et al. 2024;

[10] E. Margaret Burbridge Postdoctoral Fellow.

J. Inglis et al. 2024; M. Zhang et al. 2025). There have been a number of other tentative hints of sulfur chemistry in exoplanet atmospheres (e.g., A. Banerjee et al. 2024; B. Benneke et al. 2024; A. W. Mayo et al. 2025; E.-M. Ahrer et al. 2025; B. Davenport et al. 2025; L. Felix et al. 2025; A. Meech et al. 2025), but the number of confident detections of such species remains low.

Precisely measuring an exoplanet's sulfur content allows us to finally move beyond the hoary old C/O ratio, which has degenerate implications for planetary formation conditions; (e.g., C. Mordasini et al. 2016; P. Mollière et al. 2022; A. D. Feinstein et al. 2025). Unlike volatiles such as C or O, sulfur has a much higher condensation/vaporization temperature (K. Lodders 2003), and so it traces an exoplanet's refractory budget. S is particularly useful because it is the most volatile of the major refractory constituents. Rock and metal tracers like Fe, Mg, and Si are only observable in the hottest of planets (>2000 K; J. D. Lothringer et al. 2021) because they condense out of the atmosphere for the vast majority of giant planets. Unfortunately, these ultrahot planets are rare and also suffer from complications like molecular dissociation and ionization (J. Arcangeli et al. 2018; J. D. Lothringer et al. 2018), which make robust elemental abundances challenging. Thus, measuring sulfur in our targets represents the best chance at tracing the accretion of refractory material in giant planets (I. J. M. Crossfield 2023). Specifically, the volatile-to-refractory C/S and O/S ratios may be the key to distinguishing between pebble- or planetesimal-dominated accretion (A. D. Schneider & B. Bitsch 2021; D. Turrini et al. 2021; E. Pacetti et al. 2022) in a way that the oft-studied C/O ratio cannot (I. J. M. Crossfield 2023).

Furthermore, sulfur as a refractory tracer informs us about other solids accreted onto the planet. For example, carbon fractionation in the disk: C in disk polycyclic aromatic hydrocarbons are released into the gas phase at the so-called soot line of protoplanetary disks (M. E. Kress et al. 2010). Based on solar system meteorites, ∼50% of the disk carbon is found in the solid phase (E. A. Bergin et al. 2015), and so ice-phase carbon alone cannot provide an accurate estimate of the C budget in a disk. Ignoring the refractory carbon can result in inaccurate predictions for the planet formation based on its atomic composition. For regions where the temperature reaches 1200 K for a few hundred years, solid-phase C will be released into the gas phase; this location is typically ∼0.3–3 au (F. Binkert & T. Birnstiel 2023). Simulations predict a direct connection between the amount of solid-phase C and the planet's total C and S abundances (e.g., A. D. Feinstein et al. 2025, and references therein). Even though the chemical history and complex carbon chemistry can both cause uncertainties in the carbon fractionation inferred from sulfur abundances, only observational data can provide the tightest possible C and S constraints—which are essential to best reveal the history of planets and their natal disks.

By observing large numbers of planets and enabling the identification of SO_2 and H_2S in exoplanetary spectra (see Figure 1), JWST opens a new window into the elemental makeup and disequilibrium processes that influence giant planet compositions. In *equilibrium* chemistry SO_2 is not the main bearer of atmospheric sulfur—that is H_2S (J. Polman et al. 2023). SO_2's *photochemical* origin makes SO_2 a distinct tracer of disequilibrium chemistry processes, being sensitive to UV flux, K_{zz}, T_{int}, and global circulation (I. J. M. Crossfield 2023; S.-M. Tsai et al. 2023a, 2023b; S. Mukherjee et al. 2025; W. de Gruijter et al. 2025).

SO_2 in giant planet atmospheres also traces enhanced atmospheric metallicity (I. J. M. Crossfield 2023; S.-M. Tsai et al. 2023a). The SO_2 absorptions in the 7.4 and 8.7 μm bands are much more sensitive metallicity tracers than those at 4.1 μm, which saturate at lower metallicity (I. J. M. Crossfield 2023; S.-M. Tsai et al. 2023a). Thus longer-wavelength measurements of SO_2 are crucial to precisely measure the S content (and for the total oxygen abundance, as SO_2 locks oxygen away from CO, CO_2, and H_2O).

In this paper we calculate and present a series of atmospheric models to better elucidate the location of the exoplanetary "SO_2 shoreline"—the boundary between regions of gas giant parameter space where SO_2 is abundant enough to be detected and regions where it may go unseen. We also explore more generally the sulfur chemistry of these H_2/He-dominated atmospheres. Section 2 presents our modeling approach. Section 3 discusses these results to determine which parameters have a particularly strong or weak influence on the expected atmospheric SO_2 abundance. Section 4 then discusses the overall sulfur budget and the dominant sulfur-carrying molecules expected in exoplanet atmospheres, before concluding in Section 5.

2. Modeling

To map the exoplanetary SO_2 shoreline, we generated a suite of model atmospheres and corresponding synthetic spectra largely following the same approach as I. J. M. Crossfield (2023). Our modeling parameters are summarized in Table 1. In brief, we use `HELIOS` (M. Malik et al. 2017) to generate vertical temperature profiles in radiative–convective (but not thermochemical) equilibrium for a given bulk metallicity (M/H), semimajor axis (a, or equivalently equilibrium temperature T_{eq}), internal temperature (T_{int}), and related system parameters (S. Mukherjee et al. 2025 showed that fully self-consistent equilibrium profiles change temperatures by <10%). Figure 2 shows a subset of the resulting temperature profiles; for all models we used a single heat-recirculation efficiency of 0.5, on a scale from 0.25 to 1.0. We then use `VULCAN` (S.-M. Tsai et al. 2017) with its SNCHO chemical network to calculate vertical chemical profiles for each `HELIOS` temperature profile for a range of X-ray and ultraviolet (XUV) irradiation, C/O ratio, and vertical diffusion (K_{zz}). Finally, we use `petitRADTRANS` (P. Mollière et al. 2019) to calculate synthetic transmission spectra of the planets; the spectra include molecular opacity from H_2O, CO, CO_2, OH, SO_2, SO, CH_4, HCN, H_2S, NH_3, CH_3, C_2H_2, C_2H_4, CN, CH, SH, CS, H_2CO, H_2O_2, N_2O, NH, NO, and NS as well as atomic Na and K at each specified metallicity level. Figure 3 shows the typical cross sections of some of the key sulfur-bearing species, vertical mixing ratios for sulfur-bearing species, and a representative model transmission spectrum. References for our opacities are listed in the Appendix.

Since Na and K are not treated in `VULCAN`'s chemical network, to calculate our transmission spectra we simply scaled the abundances of these elements relative to the solar values in the same way as for C, N, O, and S. Any species including other elements beyond those listed above are not included in the atmospheric chemistry or resulting spectra. Note that our analysis also does not account for phase changes; particularly for our coolest models, H_2O condensation may

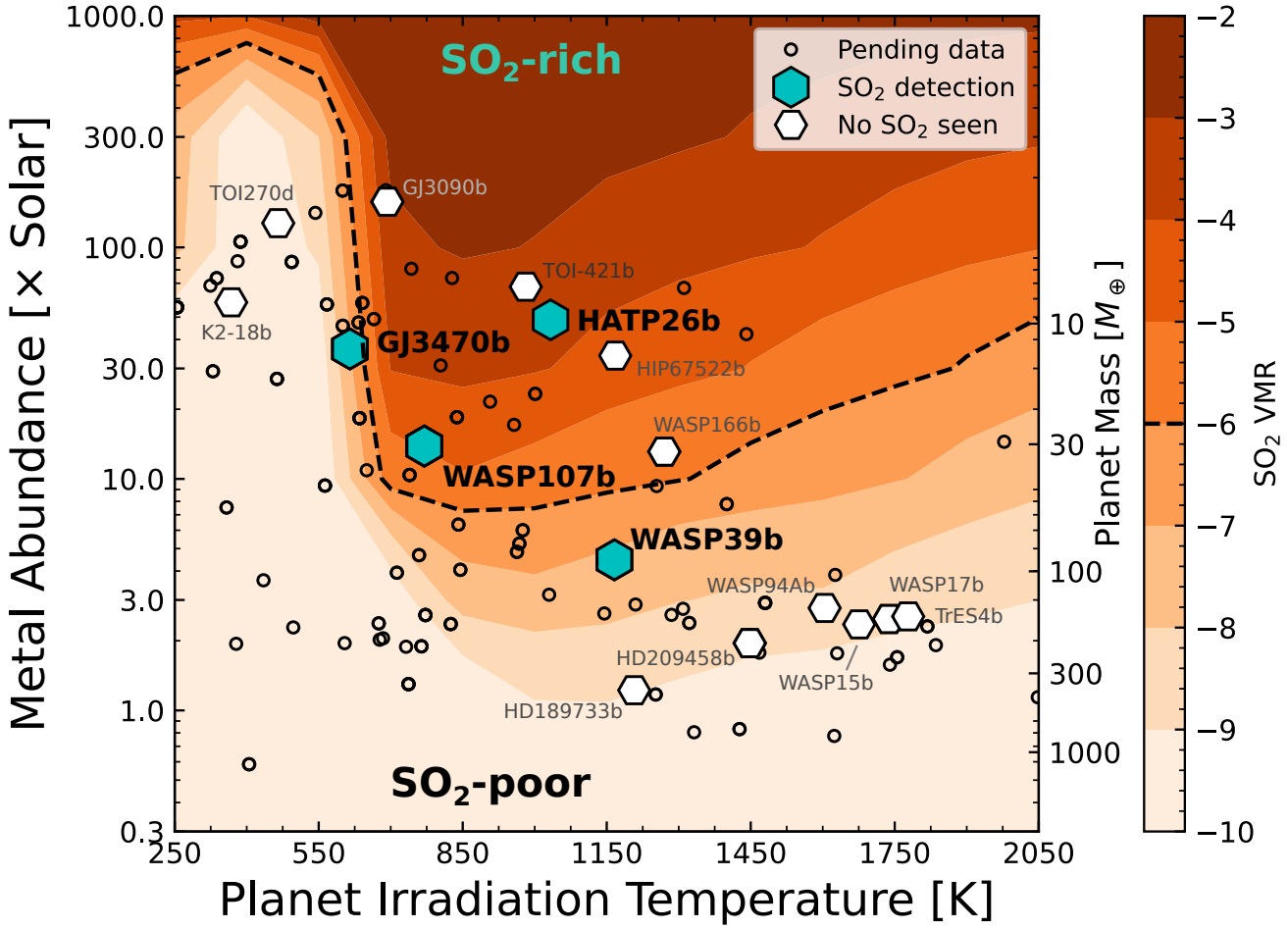

Figure 1. SO_2 abundance averaged from 1 to 100 μbar for our nominal model grid (color map), with the 1 ppm volume mixing ratio indicated by the dashed line. We term this the "SO_2 shoreline," below which SO_2 is unlikely to be detectable. Markers show the shoreline in the context of exoplanets observed by JWST in transit with $R_P \geqslant 1.8R_\oplus$. Empty symbols indicate unpublished observations, white hexagons show SO_2 nondetections, and blue hexagons show SO_2 detections. All four nondetections within the SO_2-rich region still allow for the presence of significant levels of SO_2.

result in significant changes to the atmospheric thermal structure and chemistry compared to the results we present here.

Since SO_2 has been detected in a wide range of planets, from the smallish warm Neptunes GJ 3470b to HAT-P-26b to the hot Jupiters WASP-107b and WASP-39b (L. Alderson et al. 2023; T. G. Beatty et al. 2024; D. K. Sing et al. 2024; L. Welbanks et al. 2024; J. Valenti et al. 2025, L. Alderson et al. 2025, in preparation, A. Gressier et al. 2025), in our models we adopt the properties of the intermediate-size planet HAT-P-26b. The physical system parameters we take from H. R. Wakeford et al. (2017). Our nominal stellar spectrum for the VULCAN photochemistry calculations is from the MUSCLES Extension program (K. France et al. 2016; P. R. Behr et al. 2023), which includes observed STIS spectra of HAT-P-26, with X-ray and far-ultraviolet data taken from HD 40307 (A. Youngblood et al. 2016). Our models with semimajor axis 0.0471 au (1000 K) correspond most closely to the actual planet HAT-P-26b, while the remaining models span the rest of irradiation parameter space.

The final result is several grids of model atmospheres and spectra. Our nominal grid spans 13 semimajor axes (corresponding to $T_{\rm eq}$ from 250 to 2050 K) and 8 metallicities (from 0.3× to 1000× the solar level) for an initial total of 104 models. We also calculate numerous grids in which a single parameter is changed: $T_{\rm int}$ of 300 or 500 K (versus a nominal value of 100 K); XUV irradiation at either 0.03× or 30× the nominal value; constant-with-altitude K_{zz} of 10^5 or 10^9 (nominal value 10^7); or an elemental C/O ratio of 0.30 or 0.80 instead of the nominal, solar value of 0.55. Table 1 lists all these parameters, with the nominal parameters in bold. Again, note that the lack of condensation treatment in our models may significantly impact the accuracy of the coolest set of models. All temperature profiles, chemical profiles, and synthetic spectra are available in Zenodo at doi:10.5281/zenodo.17101615.

3. Results: Tracing the SO_2 Shoreline

Figure 1 shows the exoplanetary "SO_2 shoreline," regions of temperature and metallicity where SO_2 is predicted to be abundant. The color shading indicates the predicted amount of SO_2 (averaged from 1 to 100 μbar) in the atmospheres of these planets assuming $T_{\rm int} = 100$ K, $K_{zz} = 10^7$ cm^2 s^{-1}, and C/O = 0.55. The dashed line at a volume mixing ratio of 10^{-6} roughly indicates the minimum abundance that we might hope to detect (see D. Powell et al. 2024; D. K. Sing et al. 2024).

The SO_2 shoreline is a steep function of planet temperature and metallicity (I. J. M. Crossfield 2023; J. Polman et al. 2023; S.-M. Tsai et al. 2023a). Below ~600 K the SO_2 abundance is extremely low for M/H $\lesssim$ 300× solar, but for higher

Table 1
Model Parameters

Name	Units	Description	Value	Source
System parameters				
R_*	$R_\odot$	Stellar radius	0.79	(H. R. Wakeford et al. 2017)
$T_{\rm eff}$	K	Stellar effective temperature	5062	(H. R. Wakeford et al. 2017)
R_P	$R_\oplus$	Planetary radius	6.33	(H. R. Wakeford et al. 2017)
M_P	$M_\oplus$	Planetary mass	18.73	(H. R. Wakeford et al. 2017)
g_P	m s^{-2}	Planetary surface gravity	4.58	(H. R. Wakeford et al. 2017)
Modeling parameters: constant values				
He/H	···	Solar volume mixing ratio	8.38×10^{-2}	K. Lodders (2020)
C/H	···	Solar volume mixing ratio	2.95×10^{-4}	K. Lodders (2020)
N/H	···	Solar volume mixing ratio	7.08×10^{-5}	K. Lodders (2020)
O/H	···	Solar volume mixing ratio	5.37×10^{-4}	K. Lodders (2020)
S/H	···	Solar volume mixing ratio	1.41×10^{-5}	K. Lodders (2020)
P	bar	Pressure range	1000–10^{-7}	
P_0	bar	Reference pressure	0.01	
z	deg	Zenith angle	83	
Modeling parameters: varied values				
M/H	···	Metallicity relative to solar	0.3, 1, 3, 10, 30, 100, 30, 1000	
$T_{\rm eq}$	K	Equilibrium temperature	250, 400, 550, 700, 850, 1000, 1150, 1300, 1450, 1600, 1750, 1900, 2050	
a	AU	Semimajor axis	0.753, 0.294, 0.156, 0.0960, 0.0651, 0.0471, 0.0356, 0.0278, 0.0224, 0.0184, 0.0154, 0.0130, 0.0112	
$T_{\rm int}$	K	Internal temperature	**100**, 300, 500	
$F_{\rm XUV}$	···	Relative XUV irradiation	0.03, **1.0**, 30	
K_{zz}	cm^2 s^{-1}	Vertical diffusion coefficient	10^5, **10^7**, 10^9	
C/O	···	C/O ratio	0.3, **0.55**, 0.8	

Note. Entries in **bold** indicate the values used for the nominal model.
All temperature profiles, chemical profiles, and synthetic spectra are available electronically in Zenodo at doi:10.5281/zenodo.17101615.

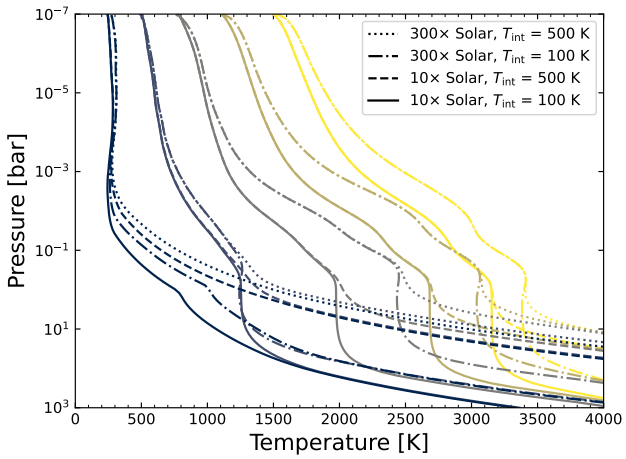

Figure 2. Representative temperature profiles of our models, showing two metallicities and two $T_{\rm int}$ for equilibrium temperatures of 250, 700, 1150, 1600, and 2050 K. Changing $T_{\rm int}$ affects the temperature profile at $P \gtrsim 1$ mbar, at altitudes below where transmission spectra probe and where SO_2 is produced.

irradiation levels SO_2 is considerably more abundant and may be detectable at metallicities as low as $\sim 3\times$ solar. We next consider how the shoreline advances or retreats as various parameters are adjusted.

Internal temperature. Atmospheric SO_2 is particularly insensitive to $T_{\rm int}$. Figure 2 shows that increasing $T_{\rm int}$ from 100 to 500 K only marginally changes the temperature profile in the upper atmosphere where SO_2 is produced. Thus, we find that the SO_2 shoreline in our nominal model ($T_{\rm int} = 100$ K) is almost indistinguishable from the shoreline predicted when $T_{\rm int} = 500$ K. This result indicates that $T_{\rm int}$ is unlikely to be a confounding factor when interpreting measured SO_2 abundances, confirming the results of S. Mukherjee et al. (2025).

Incident XUV flux. Surprisingly, we also find a relatively weak dependence of SO_2 abundance on the incident high-energy flux. Figure 4 reveals that changing the $\lambda < 230$ nm flux by a factor of 30 negligibly shifts the SO_2 shoreline for $T_{\rm eq} \gtrsim 1000$ K, with somewhat larger effects at cooler temperatures. At a given temperature and metallicity, significantly increasing the high-energy flux generally decreases the amount of atmospheric SO_2. The result is surprising, considering the stronger dependence of SO_2 on incident XUV flux reported by previous studies (A. Dyrek et al. 2024; W. de Gruijter et al. 2025), but is consistent with that found by S. Mukherjee et al. (2025). Since high-energy stellar flux is largely or entirely unmeasured for most systems where SO_2 H_2S, and other sulfur-bearing species are sought, this result implies that this uncertainty in stellar flux may have at most a modest impact on interpreting these SO_2 detections.

Vertical mixing. The impact of K_{zz} is more striking. Figure 5 reveals that varying K_{zz} by 4 orders of magnitude results in negligible changes to the SO_2 shoreline for $T_{\rm eq} \gtrsim 600$ K. However, at cooler temperatures a stark change emerges: below 600 K, a lower K_{zz} dramatically decreases the SO_2 abundance in the upper atmosphere at a given temperature and metallicity. This effect is most likely to be detectable for high-metallicity ($\gtrsim 100\times$ solar) planets with $K_{zz} \gtrsim 10^7$ cm^2 s^{-1} and $T_{\rm eq} \lesssim 600$ K. Figure 5 also hints that for $T_{\rm eq} \gtrsim 1200$ K the trend may reverse, with higher K_{zz} implying lower SO_2 abundance; however, this effect

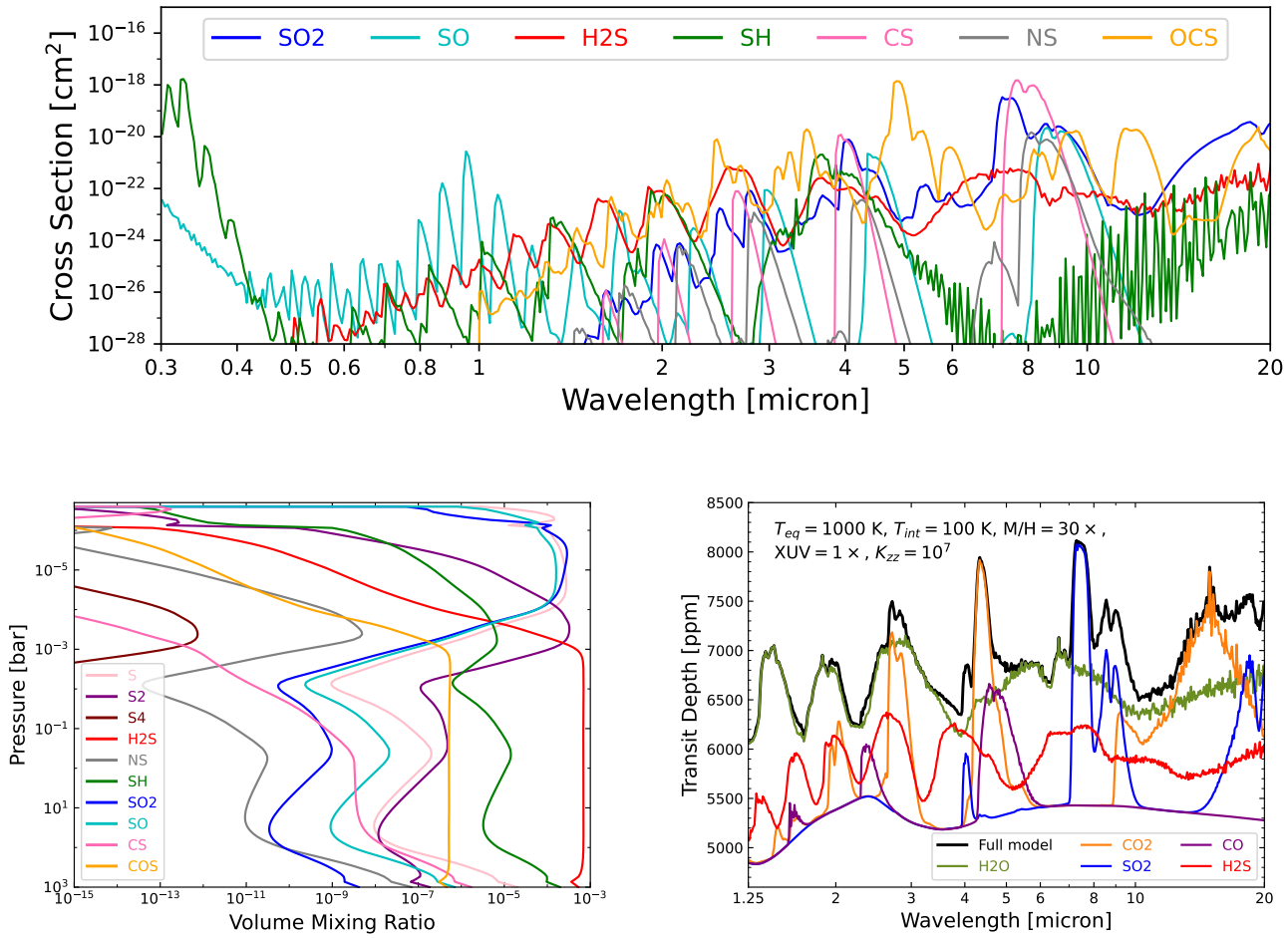

Figure 3. Top: cross sections of sulfur-bearing species, calculated at 1000 K and 10 mbar. The data have been smoothed for clarity. Bottom left: abundance profiles for $T_{\rm eq}$ = 1000 K, $T_{\rm int}$ = 100 K, 30× solar metallicity, and nominal high-energy irradiation and C/O ratio. Bottom right: full synthetic transmission spectrum (black line) together with model spectra including only one molecular absorber at a time (colored lines). Molecules not listed contribute negligibly to this spectrum.

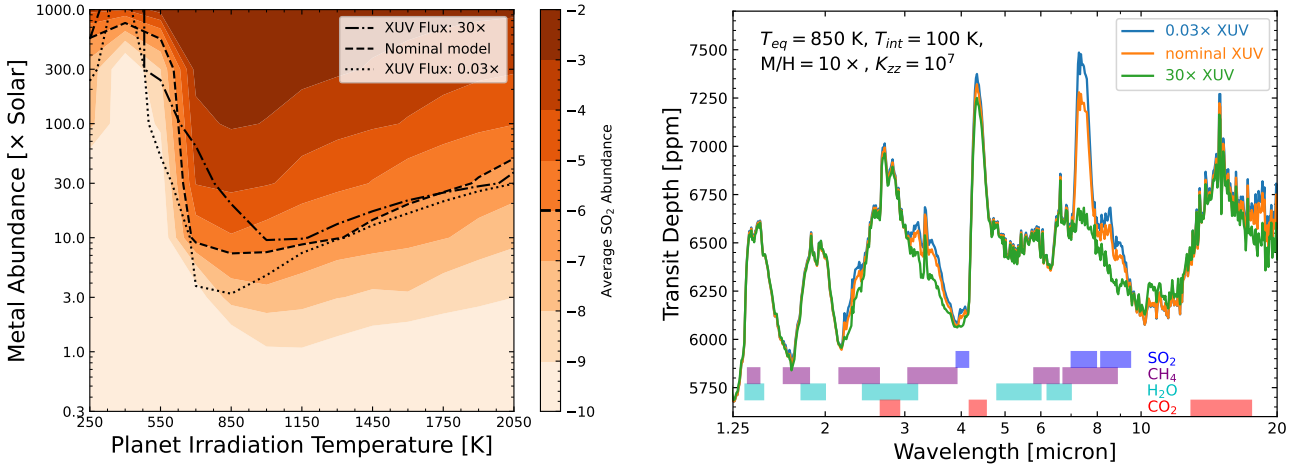

Figure 4. Left: same as Figure 1 but here showing the impact of varying the incident XUV irradiation. Significantly higher or lower levels of XUV flux can somewhat shift the SO_2 shoreline for temperatures $\lesssim$1400 K. Right: representative spectra showing that dramatically increasing the level of incident XUV results in lower levels of SO_2 (as well as CH_4).

seems weak at best, and so it may be more difficult to observationally confirm.

At equilibrium temperatures $\lesssim$600 K, SO_2 is not favored to form in significant amounts. The cause of the K_{zz} dependence at those low temperatures seems to involve sufficiently strong vertical mixing that dredges SO_2 up from deeper regions of the atmosphere (below 1 bar) where it is more plentiful than it is in the atmospheric regions probed by transmission spectroscopy. There may also be an aspect that some of the photochemically produced SO_2 is mixed downward to layers where it is less

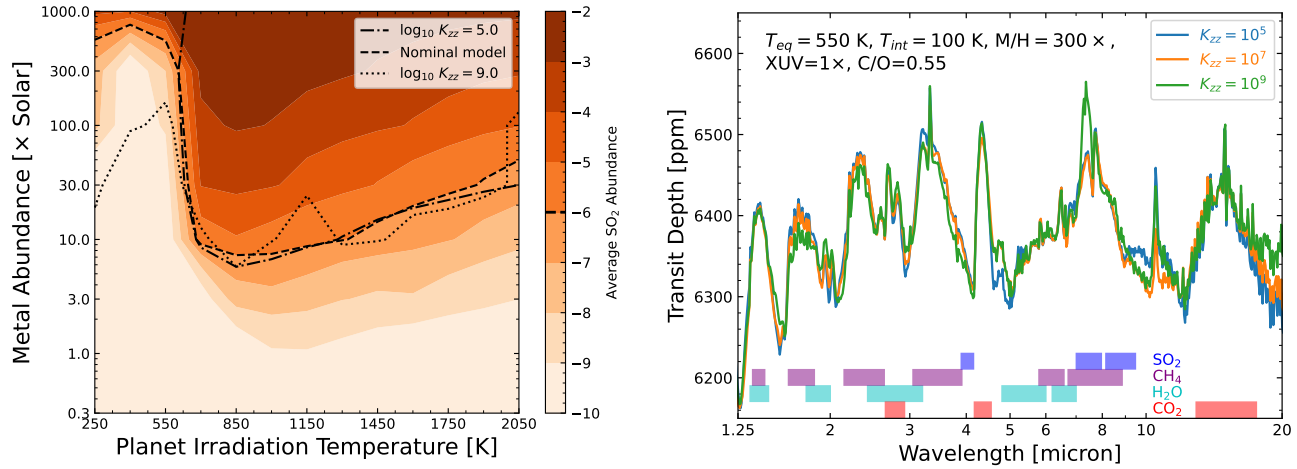

Figure 5. Same as Figure 4 but here showing the impact of varying the vertical diffusion coefficient, K_{zz}. Varying K_{zz} over 4 orders of magnitude hardly budges the SO_2 shoreline for temperatures $\gtrsim$600 K; at lower temperatures, sufficiently high K_{zz} may result in measurable SO_2 for sufficiently high metallicities. Representative spectra show that increasing K_{zz} over this range results in a slightly more detectable SO_2 signature at 7.4 μm. Note also the prominent ethylene (C_2H_4) feature at 10.5 μm.

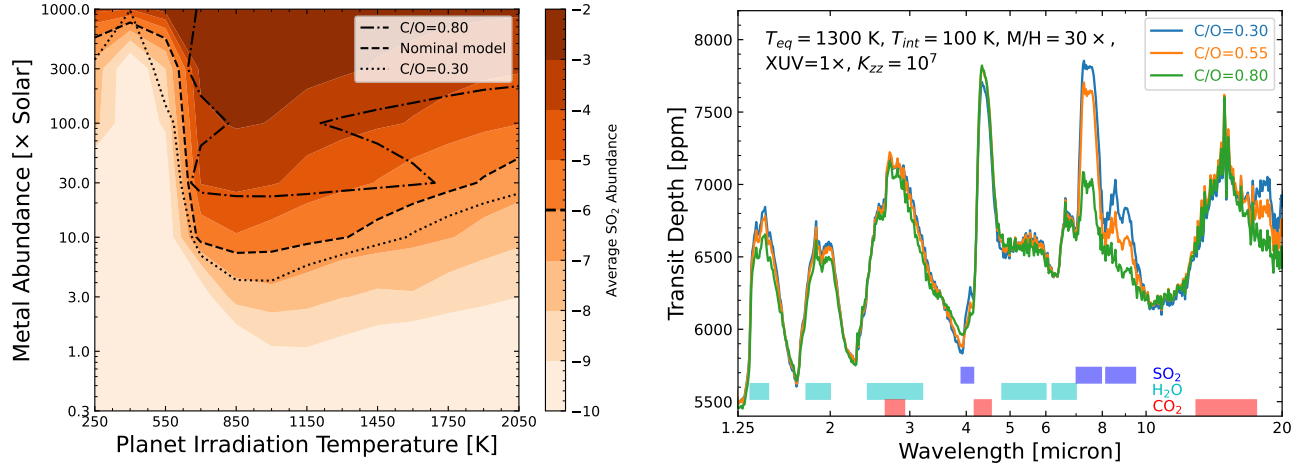

Figure 6. Left: same as Figure 1 but here showing the impact of varying the atmospheric C/O ratio. Increasing or decreasing the C/O ratio can significantly shift the SO_2 shoreline up or down, respectively. Right: representative spectra showing how decreasing the C/O ratio can significantly increase the atmospheric SO_2 signature, especially at 7.4 μm.

easily destroyed by processes in the thin upper atmosphere. The details of this dependence on vertical mixing will be the subject of a future study.

C/O ratio. Finally, Figure 6 shows that the often-sought atmospheric C/O ratio has the strongest effect on the SO_2 shoreline and overall SO_2 abundance. As the C/O ratio is increased from 0.30 to 0.80, the SO_2 abundance steadily decreases (as seen in previous studies; e.g., I. J. M. Crossfield 2023; J. Polman et al. 2023; T. G. Beatty et al. 2024; S. Mukherjee et al. 2025). Notably, the C/O ratio is the only effect we explored that shifts the SO_2 shoreline by roughly equal amounts at all planet temperatures. We also note that the shape of the shoreline appears to qualitatively change at the higher C/O ratio of 0.8; future studies may be in order to determine the cause of this change.

Regardless, the detection of SO_2 is therefore a strong sign of either a C/O ratio $\lesssim$ the solar value and/or a high overall metallicity. If most giant planets have C/O comparable to their host stars, then their C/O will be on average slightly supersolar (because the average stellar C/O is supersolar; J. J. Fortney 2012) and the planets' expected SO_2 abundances will be somewhat decreased relative to our nominal conditions (because higher C/O tends to imply lower SO_2 abundances; see Figure 6).

Finally, we note that C/O is not the only elemental ratio relevant for predicting atmospheric sulfur abundances. Ratios such as C/S or O/S (perhaps proxies for the volatile-to-refractory ratios; J. D. Lothringer et al. 2021) are also relevant for determining the atmospheric abundances of sulfur-bearing species (I. J. M. Crossfield 2023; N. Khorshid et al. 2024).

4. Where Has All the Sulfur Gone?

Figure 7 shows the overall atmospheric sulfur budget of H_2/He-dominated atmospheres across a wide range of temperatures and metallicities, as predicted by our atmospheric models. Despite the considerable attention recently directed at SO_2, in only a small subset of cases is SO_2 one of the most abundant sulfur-bearing molecules. H_2S, S_2, NS, SO, SH, and even S_8 are frequently as common (or more so) as SO_2 depending on the overall temperature and heavy element enrichment level. Contrary to S. Mukherjee et al. (2025), we do not find that CS and CS_2 ever carry a substantial fraction of

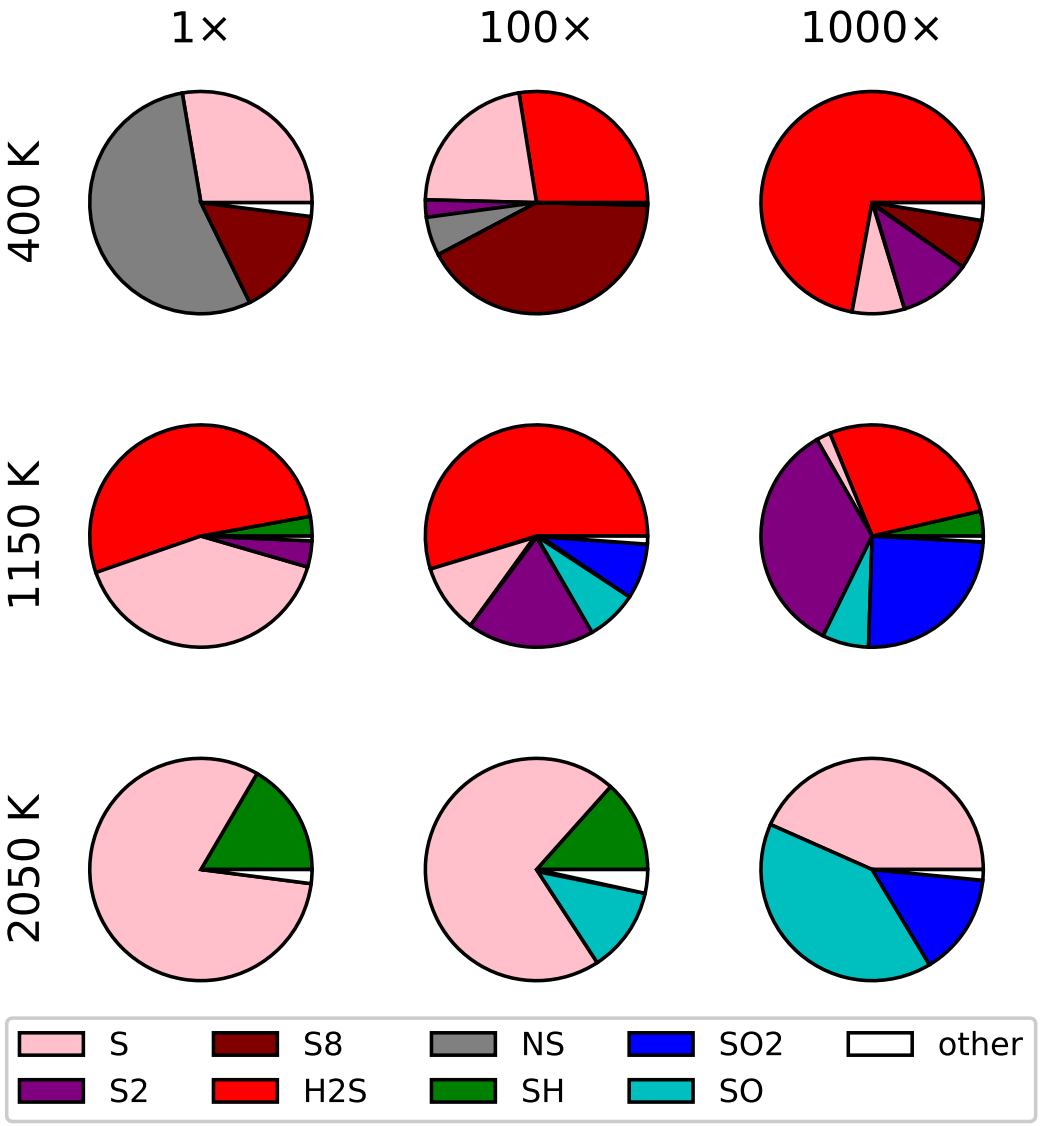

Figure 7. Each chart shows the fractional contribution of the indicated species to the overall atmospheric sulfur budget at the noted temperature and metallicity. The calculation indicates an average from 10^{-5} to 10^{-2} bar.

the atmospheric S. Note, however, that this is likely because VULCAN's chemical network currently lacks some reactions involving a subset of C–S bonded species (see J. Moses et al. 2024; R. Veillet et al. 2025). However, we do find that at lower metallicities and intermediate equilibrium temperatures (400–600 K) the sulfur that is in SO2 at higher temperatures becomes sequestered in CS_2, OCS, and S_2. At the lowest temperatures in our model grid, at low-to-moderate metallicities the sulfur is increasingly in higher-order allotropes such as S8.

Figure 3 demonstrates the relative detectability of many of these sulfur-bearing species. Consistent with previous work (e.g., J. Polman et al. 2023; S.-M. Tsai et al. 2023a), we find SO_2 to be the most readily discerned such molecule: its opacity is greatest at the 7.4 μm band (and, to a lesser extent, at 8.7 μm), but the observational signal-to-noise ratio (S/N) is typically greater at the 4.1 μm band. H_2S is often more abundant than SO_2, but strong detection of H_2S is much more challenging than for SO_2 in transmission; the best prospect may be to catch a glimpse of its broad 3.7 μm band in between the typically stronger bands of H_2O and/or CH_4 below and SO_2 and/or CO_2 above—as done for HD 189733b in transmission (G. Fu et al. 2024). Unfortunately, half of this H_2S signature lies in an unobserved detector gap when using JWST's NIRSpec/G395H mode, both partially obscuring the signal and potentially inducing systematic transit-depth offsets between the two NIRSpec detectors (see E.-M. Ahrer et al. 2025). Alternatively, H_2S is also detectable in emission spectra from 7 to 8 μm (J. Inglis et al. 2024). Finally, SO achieves appreciable abundances at higher metallicities and temperatures and may be visible from 0.8 to 1.2 μm.

5. Conclusion

5.1. Summary of Results

Sulfur chemistry remains elusive in exoplanet atmospheres. To date SO_2 has been detected in only four exoplanets. Though first observed at its 4.1 μm ($\nu_1 + \nu_3$) combination band (L. Alderson et al. 2023; Z. Rustamkulov et al. 2023; S.-M. Tsai et al. 2023a), SO_2 and the physical conditions it diagnoses also reveal themselves at the longer-wavelength 7–9 μm ν_1 and ν_3 stretch vibration bands (D. Powell et al.

2024). H_2S has been seen confidently only via emission spectroscopy, also at 7–8 μm (G. Fu et al. 2024; J. Inglis et al. 2024).

With only a handful of planets having detections of sulfur-bearing species, more observational data are urgently needed. JWST will remain the superlative facility for studying SO_2 in exoplanet atmospheres. ESA's Ariel (scheduled for launch in 2029) will also observe SO_2 in transiting exoplanet atmospheres via AIRS Channel 1, which will provide low-resolution spectra from 3.9 to 7.8 μm. These data should easily measure SO_2 at 4.1 μm, and the longest-wavelength data ($\gtrsim$7 μm) may also be sufficient to see SO_2. These facilities, and perhaps also ground-based telescopes, could also descry SO and/or SH at wavelengths below $\lesssim$1.2 μm.

Our modeling maps the expected location of the SO_2 shoreline—the boundary between atmospheres with or without detectable SO_2. Under our nominal model assumptions (Table 1) SO_2 should be detectable for $T_{eq} \gtrsim$ 600 K and metallicities $\gtrsim$10× solar. The location of the shoreline is insensitive to T_{int}, depends weakly on K_{zz} and XUV irradiation, and varies particularly strongly when the C/O ratio is adjusted. Figure 1 compares our nominal SO_2 shoreline to the properties of transiting planets being observed by JWST and finds decent agreement; however, data on more intermediate-metallicity planets (and higher-S/N data on the smallest, highest-metallicity planets) are needed to fully validate our predictions.

5.2. Discussion

Indeed, further observations of a large number of planets are the best hope for determining the true boundary of our proposed SO_2 shoreline. Figure 1 shows the SO_2 shoreline in the context of all planets being observed by JWST in transit through Cycle 4. In this figure planet mass is mapped to metallicity assuming the C/H mass–metallicity relation of L. Welbanks et al. (2019).

Of the four planets with clear SO_2 detections, three—HAT-P-26b, WASP-107b, and WASP-39b—sit within or near to the nominal SO_2 shoreline (S.-M. Tsai et al. 2023a; T. G. Beatty et al. 2024; D. Powell et al. 2024; D. K. Sing et al. 2024; L. Welbanks et al. 2024). While the previously studied WASP-39b and WASP-107b sit comfortably within or near the shoreline, GJ 3470b sits right on the edge. The possible discrepancy could be resolved if GJ 3470b's atmospheric C/O is substantially nonsolar and/or if it does not follow the putative mass–metallicity trend assumed in Figure 1.

The lower-mass planets with nondetections of SO_2 are perhaps more intriguing (Figure 1). All four lie above the SO_2 shoreline, and all show tentative hints of SO_2 just short of a significant detection. These include the 32 $M_\oplus$ WASP-166b (VMR$\sim$10 ppm; A. W. Mayo et al. 2025), the 14 $M_\oplus$ HIP 67522b (VMR $\lesssim$1 ppm; P. C. Thao et al. 2024), the 7.2 $M_\oplus$ TOI-421b (1–10 ppm; B. Davenport et al. 2025), and the low-mass (3.3 $M_\oplus$) GJ 3090b (1–100 ppm; E.-M. Ahrer et al. 2025). In all cases the precision of the reported SO_2 abundances are broad enough that the atmospheric compositions may still be generally consistent with our model predictions, but higher signal-to-noise data are needed to test our models.

Finally, the large number of massive hot Jupiters (e.g., J. Kirk et al. 2025; E.-M. Ahrer et al. 2025) lacking definitive SO_2 detections seems consistent with the model outlined in Figure 1. If this population of large, massive planets is consistently low metallicity then we may expect little or no detectable SO_2 in many of the largest, highest-S/N exoplanetary targets.

Besides comparing to individual planets, our models here will also support research efforts on other exoplanetary fronts. Our grid provides 72 model atmospheres and corresponding spectra at $T_{eq} = 1000$ K, appropriate for interpreting upcoming JWST spectroscopy of the wide range of planets marked in Figure 1. Our total grid includes 936 models, which may be a sufficiently large set to enable testing of machine learning approaches on exoplanetary chemistry and spectra across a wide range of parameter space.

5.3. Future Work and Caveats

Beyond these results, our work leaves room for improvement on several fronts.

First, our models include no clouds or hazes; such materials can significantly impact a planet's resulting transmission spectrum, as well as sequestering elements out of the gas phase into solids. The most likely sulfur-bearing condensate clouds are ZnS, MnS, and Na_2S (although there are also good reasons to think that the latter two do not form). The formation of such condensates is limited by the abundance of the trace metals Zn, Mn, and Na; the process will typically deplete $\lesssim$10% of the bulk sulfur, but not typically enough to significantly alter the atmospheric SO_2 abundance (S.-M. Tsai et al. 2023a; S. Mukherjee et al. 2025). Sulfur polymerized into the S_8 molecule can form hazes for $T_{eq} \lesssim$ 700 K, at least at near-solar metallicities (P. Gao et al. 2017); though by itself not enough to appreciably change a planet's atmospheric sulfur budget, condensation of this allotrope might even result in significant reduction in sulfur-species abundances above the haze layer.

Phase changes of H_2O were also not included in our current analysis, even though Figure 2 shows that for our coolest models, atmospheric temperatures drop below the condensation temperature of H_2O. Such phenomena are likely to have a significant impact on both the thermal structure and chemistry of these atmospheres, and so this set of models and their associated chemistry and spectra may differ substantially from the results of a more complete and self-consistent analysis.

In a related direction, our use of VULCAN's SNCHO chemical network restricts the applicability of our results in regions of parameter space where reactions with other elements are important. Thus the silicate-bearing clouds inferred for a growing number of hot Jupiters (A. Dyrek et al. 2024; J. Inglis et al. 2024) remain unaccounted for in our analysis. Recent claims of silicon-bearing gas-phase chemistry in H_2-dominated atmospheres (S. Ma et al. 2025) are untested with our current framework, as are the effects of TiO and other molecules bearing heavier atoms (see B. Prinoth et al. 2022). Furthermore, VULCAN's chemical network currently lacks some C–S bonded species, which may result in an overestimate of SO_2 at cooler temperatures where C–S species could take up a larger fraction of the sulfur (S. Mukherjee et al. 2025; R. Veillet et al. 2025). The details of the SO_2 shoreline may change somewhat when considering those relevant reactions.

Furthermore, our approach is not fully self-consistent inasmuch as each model's chemistry is computed assuming a fixed, input thermal profile. In reality the thermal profile and atmospheric composition necessarily evolve together: when

one changes, the other changes as well. As S. Mukherjee et al. (2025) point out, the effects of this choice are not fatal when considering transmission spectra and overall trends in exoplanetary atmospheric abundances.

Our treatment of atmospheric chemistry with one-dimensional models is overly simplistic since planets are, of course, three-dimensional. Models linking atmospheric dynamics to chemistry indicate that atmospheric abundances can change significantly between the morning and evening terminator, to say nothing of differences seen at other longitudes (E. K. H. Lee et al. 2023; S.-M. Tsai et al. 2024). Similar studies could also test current models by simulating the time-dependent atmospheric chemistry expected in planets on eccentric orbits (e.g., N. K. Lewis et al. 2013; S.-M. Tsai et al. 2023c).

Analyses such as ours should also be extended to a wider range of planet surface gravities than the single, HAT-P-26b-like, case explored here (or the WASP-39b-like gravity used in the model grids of I. J. M. Crossfield 2023; S. Mukherjee et al. 2025). Lower surface gravity can itself result in the formation of additional SO_2, since in such atmospheres the physically thicker atmosphere can provide additional shielding against SO_2 photodissociation (W. de Gruijter et al. 2025).

Uncertainties also remain as to the exact photochemical pathways setting the observable sulfur species. W. de Gruijter et al. (2025) only recently identified a new pathway for SO_2 formation beyond that initially reported (J. Polman et al. 2023; S.-M. Tsai et al. 2023a). Additional explorations in this direction, whether for SO_2 or other species, could be fruitful.

There is also the need for considerably more laboratory and theoretical calculations, since our model spectra still lack several key opacity sources and/or reaction rates. Opacity data exist for H_2CS, but it is not present in VULCAN's SNCHO chemical network. Many more molecules are in the network but lack opacity data in public databases such as ExoMol or DACE: S_2, S_3, S_4, S_8, HS_2, HCS, HSO, HSO_3, H_2SO_4, CH_3S, CH_3SH, and S_2O. Moreover, other sulfur-bearing molecules, such as sulfanes and hydropolysulfide (H_2S_n) may also be relevant (K. Zahnle et al. 2009) in some regions of planetary parameter space. Obtaining such reaction-rate and opacity data in a format compatible with public modeling tools will be essential to determine the relative importance and detectability of all sulfur-bearing species.

Acknowledgments

We thank the anonymous referee, as well as Dr. J. Moses, for useful comments and suggestions that significantly improved the final manuscript. We also thank Drs. L. Alderson, Th. Beatty, and J. Valenti for the useful discussions at the 2025 ExoClimes conference.

J.P. acknowledges the financial support of the SNSF under grant 51NF40_205606.

C.P.-G. acknowledges support from the E. Margaret Burbidge Prize Postdoctoral Fellowship from the Brinson Foundation.

Facilities: JWST.

Software: VULCAN (S.-M. Tsai et al. 2017), petitRADTRANS (P. Mollière et al. 2019), HELIOS (M. Malik et al. 2017).

Appendix

Table 2 lists the sources used for our molecular opacities. Most of these were taken from the ExoMol project (K. L. Chubb et al. 2020), with a smaller number from MoLLIST (P. F. Bernath 2020) and one (NO) from HITEMP (L. Rothman et al. 2010).

Table 2
Opacity Sources

Molecule	References
CH	T. Masseron et al. (2014)
CH_3	A. Y. Adam et al. (2019)
CH_4	S. N. Yurchenko & J. Tennyson (2014)
C_2H_2	K. L. Chubb et al. (2020)
C_2H_4	B. P. Mant et al. (2018)
CN	J. S. A. Brooke et al. (2014)
CO	G. Li et al. (2015)
CO_2	S. N. Yurchenko et al. (2020)
CS	G. Paulose et al. (2015)
HCN	R. J. Barber et al. (2014)
H_2CO	A. F. Al-Refaie et al. (2015)
H_2O	O. L. Polyansky et al. (2018)
H_2O_2	A. F. Al-Refaie et al. (2016)
H_2S	A. A. A. Azzam et al. (2016)
NH	J. S. A. Brooke et al. (2014, 2015)
NH_3	P. A. Coles et al. (2019)
NO	L. Rothman et al. (2010)
N_2O	S. N. Yurchenko et al. (2024a)
NS	S. N. Yurchenko et al. (2018)
OH	J. S. Brooke et al. (2016)
SH	S. N. Yurchenko et al. (2018)
SO	R. P. Brady et al. (2024)
SO_2	D. S. Underwood et al. (2016)

While tabulating these opacity sources we identified several line lists with more up-to-date line lists or opacity sources recommended for use by the ExoMol project. These are CH_4 (recommended: S. N. Yurchenko et al. 2024b), CN (recommended: A.-M. Syme & L. K. McKemmish 2020; J. S. A. Brooke et al. 2014), NO (recommended: Q. Qu et al. 2021), OH (recommended: G. B. Mitev et al. 2025), and SH (recommended: M. N. Gorman et al. 2019).

The work presented here is similar in nature to that presented recently by S. Mukherjee et al. (2025). Both efforts use grids of forward models to explore the dependence of atmospheric chemistry in H_2/He-dominated atmospheres on various parameters. Here we list some of the more salient differences in the two studies' modeling approaches.

1. *Modeled system.* We use HAT-P-26b as our fiducial model, while they use WASP-39b.
2. *Temperature range.* We span from 250 to 2050 K, while they span a narrower range of 400–1600 K.
3. *Internal temperature.* We test only three values (100, 300, 500 K), while they test five values from 30 to 500 K.
4. *Temperature profiles.* We calculate our profiles at a range of metallicities, from 0.3 to 1000× solar abundances; they generate their profiles assuming the same abundance in all cases, namely, 10× solar.
5. *Vertical diffusion (K_{zz}).* We explore just three values of K_{zz}: 10^5, 10^7, and 10^9 cm^2 s^{-1}, with the middle value our nominal case; in contrast, they explore eight values evenly separated in log-space from 10^6 to 10^{13} cm^2 s^{-1} and use 10^9 cm^2 s^{-1} as the nominal, base case.
6. *Photochemistry.* We run our photochemical models to steady state throughout the entire modeled atmosphere; they use a hybrid modeling approach assuming deep

chemical equilibrium but with photochemistry dominating at higher altitudes.

7. *XUV flux.* We explore a range of high-energy irradiation with three stellar spectra spanning 3 orders of magnitude in XUV flux, and that flux is further scaled based on the modeled semimajor axis; S. Mukherjee et al. (2025) assume a single stellar XUV spectrum and do not scale the XUV flux incident on the planet with semimajor axis.
8. *Both studies also use different, independent modeling toolkits*. We use `HELIOS` (M. Malik et al. 2017) for our temperature profiles, `VULCAN` (S.-M. Tsai et al. 2017) for our photochemistry, and `petitRADTRANS` (P. Mollière et al. 2019) to generate synthetic spectra; S. Mukherjee et al. (2025) use `PICASO` (N. E. Batalha et al. 2019), `PhotoChem` (N. Wogan 2023), and `PICASO` (S. Mukherjee et al. 2023), respectively, for those tasks.
9. Finally, that study is broader in scope, while here we provide a deeper exploration focused specifically on atmospheric sulfur chemistry.

ORCID iDs

Eva-Maria Ahrer https://orcid.org/0000-0003-0973-8426
Jonathan Brande https://orcid.org/0000-0002-2072-6541
Laura Kreidberg https://orcid.org/0000-0003-0514-1147
Joshua Lothringer https://orcid.org/0000-0003-3667-8633
Caroline Piaulet-Ghorayeb https://orcid.org/0000-0002-2875-917X
Jesse Polman https://orcid.org/0009-0009-8749-9513
Luis Welbanks https://orcid.org/0000-0003-0156-4564
James Kirk https://orcid.org/0000-0002-4207-6615
Diana Powell https://orcid.org/0000-0002-4250-0957
Niloofar Khorshid https://orcid.org/0000-0001-8427-9173

References

Adam, A. Y., Yachmenev, A., Yurchenko, S. N., & Jensen, P. 2019, JPCA, 123, 4755
Ahrer, E.-M., Gandhi, S., Alderson, L., et al. 2025, MNRAS, 540, 2535
Ahrer, E.-M., Radica, M., Piaulet-Ghorayeb, C., et al. 2025, ApJL, 985, L10
Alderson, L., Wakeford, H. R., Alam, M. K., et al. 2023, Natur, 614, 664
Al-Refaie, A. F., Polyansky, O. L., Ovsyannikov, R. I., Tennyson, J., & Yurchenko, S. N. 2016, MNRAS, 461, 1012
Al-Refaie, A. F., Yachmenev, A., Tennyson, J., & Yurchenko, S. N. 2015, MNRAS, 448, 1704
Arcangeli, J., Désert, J.-M., Line, M. R., et al. 2018, ApJL, 855, L30
Azzam, A. A. A., Tennyson, J., Yurchenko, S. N., & Naumenko, O. V. 2016, MNRAS, 460, 4063
Banerjee, A., Barstow, J. K., Gressier, A., et al. 2024, ApJL, 975, L11
Barber, R. J., Strange, J. K., Hill, C., et al. 2014, MNRAS, 437, 1828
Batalha, N. E., Marley, M. S., Lewis, N. K., & Fortney, J. J. 2019, ApJ, 878, 70
Beatty, T. G., Welbanks, L., Schlawin, E., et al. 2024, ApJL, 970, L10
Behr, P. R., France, K., Brown, A., et al. 2023, AJ, 166, 35
Benneke, B., Roy, P.-A., Coulombe, L.-P., et al. 2024, arXiv:2403.03325
Bergin, E. A., Blake, G. A., Ciesla, F., Hirschmann, M. M., & Li, J. 2015, PNAS, 112, 8965
Bernath, P. F. 2020, JQSRT, 240, 106687
Binkert, F., & Birnstiel, T. 2023, MNRAS, 520, 2055
Brady, R. P., Yurchenko, S. N., Tennyson, J., & Kim, G.-S. 2024, MNRAS, 527, 6675
Brooke, J. S., Bernath, P. F., Western, C. M., et al. 2016, JQSRT, 168, 142
Brooke, J. S. A., Bernath, P. F., & Western, C. M. 2015, JChPh, 143, 026101
Brooke, J. S. A., Bernath, P. F., Western, C. M., van Hemert, M. C., & Groenenboom, G. C. 2014, JChPh, 141, 054310
Brooke, J. S. A., Ram, R. S., Western, C. M., et al. 2014, ApJS, 210, 23
Chubb, K. L., Tennyson, J., & Yurchenko, S. N. 2020, MNRAS, 493, 1531
Coles, P. A., Yurchenko, S. N., & Tennyson, J. 2019, MNRAS, 490, 4638
Constantinou, S., Madhusudhan, N., & Gandhi, S. 2023, ApJL, 943, L10
Crossfield, I. J. M. 2023, ApJL, 952, L18
Davenport, B., Kempton, E. M. R., Nixon, M. C., et al. 2025, ApJL, 984, L44
de Gruijter, W., Tsai, S.-M., Min, M., et al. 2025, A&A, 693, A132
Dyrek, A., Min, M., Decin, L., et al. 2024, Natur, 625, 51
Feinstein, A. D., Booth, R. A., Bergner, J. B., et al. 2025, arXiv:2506.00669
Felix, L., Kitzmann, D., Demory, B.-O., & Mordasini, C. 2025, A&A, 701, A296
Fortney, J. J. 2012, ApJL, 747, L27
France, K., Parke Loyd, R. O., Youngblood, A., et al. 2016, ApJ, 820, 89
Fu, G., Welbanks, L., Deming, D., et al. 2024, Natur, 632, 752
Gao, P., Marley, M. S., Zahnle, K., Robinson, T. D., & Lewis, N. K. 2017, AJ, 153, 139
Gorman, M. N., Yurchenko, S. N., & Tennyson, J. 2019, MNRAS, 490, 1652
Gressier, A., Batalha, N. E., Wogan, N., et al. 2025, AJ, 170, 292
Inglis, J., Batalha, N. E., Lewis, N. K., et al. 2024, ApJL, 973, L41
Khorshid, N., Min, M., Polman, J., & Waters, L. B. F. M. 2024, A&A, 685, A64
Kirk, J., Ahrer, E.-M., Claringbold, A. B., et al. 2025, MNRAS, 537, 3027
Kress, M. E., Tielens, A. G. G. M., & Frenklach, M. 2010, AdSpR, 46, 44
Lee, E. K. H., Tsai, S.-M., Hammond, M., & Tan, X. 2023, A&A, 672, A110
Lewis, N. K., Knutson, H. A., Showman, A. P., et al. 2013, ApJ, 766, 95
Li, G., Gordon, I. E., Rothman, L. S., et al. 2015, ApJS, 216, 15
Lodders, K. 2003, ApJ, 591, 1220
Lodders, K. 2020, Oxford Research Encyclopedia of Planetary Science (Oxford: Oxford Univ. Press)
Lothringer, J. D., Barman, T., & Koskinen, T. 2018, ApJ, 866, 27
Lothringer, J. D., Rustamkulov, Z., Sing, D. K., et al. 2021, ApJ, 914, 12
Ma, S., Saba, A., Faris Al-Refaie, A., et al. 2025, arXiv:2504.07823
Malik, M., Grosheintz, L., Mendonça, J. M., et al. 2017, AJ, 153, 56
Mant, B. P., Yachmenev, A., Tennyson, J., & Yurchenko, S. N. 2018, MNRAS, 478, 3220
Masseron, T., Plez, B., Van Eck, S., et al. 2014, A&A, 571, A47
Mayo, A. W., Fortenbach, C. D., Louie, D. R., et al. 2025, AJ, 170, 50
Meech, A., Claringbold, A. B., Ahrer, E.-M., et al. 2025, MNRAS, 539, 1381
Mitev, G. B., Bowesman, C. A., Zhang, J., Yurchenko, S. N., & Tennyson, J. 2025, MNRAS, 536, 3401
Mollière, P., Molyarova, T., Bitsch, B., et al. 2022, ApJ, 934, 74
Mollière, P., Wardenier, J. P., van Boekel, R., et al. 2019, A&A, 627, A67
Mordasini, C., van Boekel, R., Mollière, P., Henning, T., & Benneke, B. 2016, ApJ, 832, 41
Moses, J., Tsai, S.-M., Fortney, J., et al. 2024, AAS/DPS Meeting, 56, 308.06
Mukherjee, S., Batalha, N. E., Fortney, J. J., & Marley, M. S. 2023, ApJ, 942, 71
Mukherjee, S., Fortney, J. J., Wogan, N. F., Sing, D. K., & Ohno, K. 2025, ApJ, 985, 209
Pacetti, E., Turrini, D., Schisano, E., et al. 2022, ApJ, 937, 36
Paulose, G., Barton, E. J., Yurchenko, S. N., & Tennyson, J. 2015, MNRAS, 454, 1931
Polman, J., Waters, L. B. F. M., Min, M., Miguel, Y., & Khorshid, N. 2023, A&A, 670, A161
Polyansky, O. L., Kyuberis, A. A., Zobov, N. F., et al. 2018, MNRAS, 480, 2597
Powell, D., Feinstein, A. D., Lee, E. K. H., et al. 2024, Natur, 626, 979
Prinoth, B., Hoeijmakers, H. J., Kitzmann, D., et al. 2022, NatAs, 6, 449
Qu, Q., Yurchenko, S. N., & Tennyson, J. 2021, MNRAS, 504, 5768
Rothman, L., Gordon, I., Barber, R., et al. 2010, JQSRT, 111, 2139
Rustamkulov, Z., Sing, D. K., Mukherjee, S., et al. 2023, Natur, 614, 659
Schneider, A. D., & Bitsch, B. 2021, A&A, 654, A72
Sing, D. K., Rustamkulov, Z., Thorngren, D. P., et al. 2024, Natur, 630, 831
Syme, A.-M., & McKemmish, L. K. 2020, MNRAS, 499, 25
Thao, P. C., Mann, A. W., Feinstein, A. D., et al. 2024, AJ, 168, 297
Tsai, S.-M., Lee, E. K. H., Powell, D., et al. 2023a, Natur, 617, 483
Tsai, S.-M., Lyons, J. R., Grosheintz, L., et al. 2017, ApJS, 228, 20
Tsai, S.-M., Moses, J. I., Powell, D., & Lee, E. K. H. 2023b, ApJL, 959, L30
Tsai, S.-M., Parmentier, V., Mendonça, J. M., et al. 2024, ApJ, 963, 41
Tsai, S.-M., Steinrueck, M., Parmentier, V., Lewis, N., & Pierrehumbert, R. 2023c, MNRAS, 520, 3867
Turrini, D., Schisano, E., Fonte, S., et al. 2021, ApJ, 909, 40
Underwood, D. S., Tennyson, J., Yurchenko, S. N., et al. 2016, MNRAS, 459, 3890
Valenti, J., Lewis, N., Gressier, A., et al. 2025, ExoClimes, Vol. 1, ExoClimes VII, Poster, 9
Veillet, R., Venot, O., Sirjean, B., et al. 2025, arXiv:2505.12152

Wakeford, H. R., Sing, D. K., Kataria, T., et al. 2017, Sci, 356, 628
Welbanks, L., Bell, T. J., Beatty, T. G., et al. 2024, Natur, 630, 836
Welbanks, L., Madhusudhan, N., Allard, N. F., et al. 2019, ApJL, 887, L20
Wogan, N., 2023 PhotochemPy: 1-D photochemical model of rocky planet atmospheres, Astrophysics Source Code Library, ascl:2312.011
Youngblood, A., France, K., Loyd, R. O. P., et al. 2016, ApJ, 824, 101
Yurchenko, S. N., Bond, W., Gorman, M. N., et al. 2018, MNRAS, 478, 270
Yurchenko, S. N., Mellor, T. M., Freedman, R. S., & Tennyson, J. 2020, MNRAS, 496, 5282
Yurchenko, S. N., Mellor, T. M., & Tennyson, J. 2024a, MNRAS, 534, 1364
Yurchenko, S. N., Owens, A., Kefala, K., & Tennyson, J. 2024b, MNRAS, 528, 3719
Yurchenko, S. N., & Tennyson, J. 2014, MNRAS, 440, 1649
Zahnle, K., Marley, M. S., & Fortney, J. J. 2009, arXiv:0911.0728
Zhang, M., Paragas, K., Bean, J. L., et al. 2025, AJ, 169, 38